PNAS RESEARCH ARTICLE | NEUROSCIENCE OPEN ACCESS

Poly-dipeptides produced from *C9orf72* hexanucleotide repeats cause selective motor neuron hyperexcitability in ALS

Yunhee Jo[a,1], Jiwon Lee[b,1], Seul-Yi Lee[a,1], Ilmin Kwon[b,2], and Hana Cho[a,2]

Edited by Lily Jan, HHMI, University of California, San Francisco, CA; received July 27, 2021; accepted January 11, 2022

Expansion of the GGGGCC hexanucleotide repeat in the chromosome 9 open reading frame 72 (*C9orf72*) gene is the most common genetic cause of amyotrophic lateral sclerosis (ALS). As in other forms of ALS, selective hyperexcitability of the motor cortex has been implicated as a cause of the motor neuron death in *C9orf72*-associated ALS. Here, we show that proline–arginine (PR) poly-dipeptides generated from *C9orf72* repeat expansions increase the intrinsic excitability in pyramidal neurons of the motor cortex but not in the principal neurons of the visual cortex, somatosensory cortex, or hippocampus. We further show that this effect is attributable to PR-induced enhancement of the persistent sodium current primarily through an Nav1.2-β1-β4 complex. Reconstitution assays reveal that an auxiliary subunit, β4, plays a crucial role in the PR-mediated modulation of human Nav1.2 channel activity. Moreover, compared with the visual cortex, binding of PR poly-dipeptide to Nav1.2 is stronger in the motor cortex, where β4 is highly expressed. Taken together, these studies suggest a cellular mechanism underlying cortical hyperexcitability in *C9orf72* ALS by providing evidence that PR poly-dipeptides induce hyperexcitability in cortical motor neurons by modulating the Nav1.2 channel complex.

C9orf72 ALS | PR poly-dipeptides | motor neuron | hyperexcitability | sodium channels

Significance

The GGGGCC hexanucleotide repeat expansion in the chromosome 9 open reading frame 72 (*C9orf72*) gene is the most common genetic cause of amyotrophic lateral sclerosis (ALS). Despite myriad studies on the toxic effects of poly-dipeptides produced from the *C9orf72* repeats, the mechanisms underlying the selective hyperexcitability of motor cortex that characterizes the early stages of *C9orf72* ALS patients remain elusive. Here, we show that the proline–arginine poly-dipeptides cause hyperexcitability in cortical motor neurons by increasing persistent sodium currents conducted by the Nav1.2/β4 sodium channel complex, which is highly expressed in the motor cortex. These findings provide the basis for understanding how the *C9orf72* mutation causes motor neuron hyperactivation that can lead to the motor neuron death in *C9orf72* ALS.

Expansion of the GGGGCC hexanucleotide repeat in the first intron of the chromosome 9 open reading frame 72 (*C9orf72*) gene is implicated in most cases of familial amyotrophic lateral sclerosis (ALS), as well as in ∼10% of instances of sporadic ALS (1, 2). Three main mechanisms have been proposed to underlie the pathogenesis of *C9orf72*-associated ALS. One involves the presence of a large GGGGCC repeat expansion that would lead to the down-regulation of *C9orf72* gene expression and the loss of its normal cellular function (3). Another is associated with the accumulation of sense G4C2 and antisense G2C4 repeat–containing RNA, which could lead to the creation of toxic nuclear aggregates, resulting in the sequestration of essential RNA binding proteins, including splicing factors, with consequential defects in pre-messenger RNA (mRNA) splicing (4). In the last, one or more of the poly-dipeptides generated via repeat-associated non-ATG–initiated translation, also termed RAN translation, are proposed to be toxic to nerve cells (5, 6). This unconventional translation results in the production of five different poly-dipeptides depending on reading frames, namely poly-glycine–alanine, poly-glycine–proline, poly-GR (glycine–arginine), poly-proline–alanine, and poly-PR (proline–arginine) (7–13). Several studies have reported that poly-PR and poly-GR peptides exert toxicity via broad impediments to RNA biogenesis (5–7) and cellular organization (14). Specifically, the application of synthetic poly-PR peptides to human astrocytes induces the same missplicing of the glutamate transporter *EAAT2* transcript as that found in *C9orf72* ALS patients (5, 15). Decreased EAAT2 levels and reduced glutamate reuptake from the synaptic cleft have been hypothesized to cause glutamate-mediated excitotoxicity in ALS patients (16). However, no study to date has linked repeat expansion to the selective vulnerability of motor neurons, suggesting that the repeat expansion in *C9orf72* triggers additional and as yet unidentified pathogenic events.

Motor cortex (M1) hyperexcitability has been established as an early and prominent feature in *C9orf72* ALS patients (17–19). Recent studies have shown that cortical hyperexcitability could be useful as a diagnostic biomarker for ALS, particularly at an early stage of the disease (16). Interestingly, this cortical hyperexcitability precedes the onset of motor symptoms (16, 20), which suggests that it is involved in ALS pathogenesis rather than simply acting as a marker of the disease. In vitro studies using human-induced pluripotent stem cell–derived motor neurons harboring *C9orf72* mutations confirmed that hyperexcitability onset occurs before any overt changes in cell viability, implying that it contributes to the earliest events that ultimately lead to irreversible neurodegeneration in *C9orf72* ALS patients (21). Nevertheless, the pathophysiological

Author affiliations: [a]Department of Physiology, Sungkyunkwan University School of Medicine, Suwon 16419, Korea; and [b]Department of Anatomy and Cell Biology, Sungkyunkwan University School of Medicine, Suwon 16419, Korea

Author contributions: I.K. and H.C. designed research; Y.J., J.L., and S.-Y.L. performed research; Y.J., J.L., I.K., and H.C. analyzed data; and I.K. and H.C. wrote the paper.

The authors declare no competing interest.

This article is a PNAS Direct Submission.

[1]Y.J., J.L., and S.-Y.L. contributed equally to this work.

[2]To whom correspondence may be addressed. Email: ilmin.kwon@skku.edu or hanacho@skku.edu.

This article contains supporting information online at http://www.pnas.org/lookup/suppl/doi:10.1073/pnas.2113813119/-/DCSupplemental.

Published March 8, 2022.

mechanism by which the *C9orf72* repeat expansion leads to cortical hyperexcitability remains unknown.

Because hyperexcitable neurons are vulnerable to glutamate toxicity (16, 20), we hypothesized that toxic poly-dipeptides produced from the *C9orf72* mutation might trigger hyperexcitability selectively in motor neurons. To test this, we introduced synthetic PR poly-dipeptides into different types of neurons in acute brain slices while undertaking patch-clamp recordings of neuronal activity. This allowed us to track dynamic changes in electrical activity in living cells upon poly-dipeptide application, identify neuron subtypes with distinct electrophysiological characteristics, and ascertain the toxic effects exerted by poly-dipeptides produced from *C9orf72* repeat expansion. We found that the *C9orf72*-derived poly-dipeptides induced hyperexcitability in motor neurons by binding to, and hyperactivating, a voltage-gated sodium channel (Nav) Nav1.2. The sensitivity of Nav1.2 to the poly-dipeptides was mediated through an auxiliary β4-subunit that is highly expressed in the M1. Together, these data reveal a possible cellular mechanism underlying how *C9orf72* repeats induce hyperexcitability in motor neurons in the brain, an effect that might initiate a process of selective motor neuron death in *C9orf72* ALS patients.

Results

The proline-arginine $(PR)_{20}$ Poly-Dipeptides Induced Hyperexcitability in Cortical Motor Neurons. To examine the direct action of soluble PR poly-dipeptides on neurons of acute brain slices, we prepared synthetic peptide containing 20 repeats of the PR sequence (PR_{20}) as previously described (5). The synthesized PR_{20} peptide was soluble in both standard artificial cerebrospinal fluid (aCSF) and the internal pipette solution (*Materials and Methods*) up to a concentration of 1 μM. To mimic the endogenously generated PR poly-dipeptide, we first injected different concentrations of the PR_{20} peptide into the cytosol of layer 5 (L5) pyramidal cells (PCs) of the primary M1–cortical motor neurons through a patch pipette, while neuronal activity was evaluated using current-clamp recordings in the presence of synaptic transmission blockers (*Materials and Methods*). As shown in *SI Appendix*, Fig. S1 *A–F*, the application of the PR_{20} peptide induced a marked and dose-dependent increase in action potential (AP) firing evoked by depolarizing current steps in M1 motor neurons, reaching a steady state within 3 min after patch break-in. Because the PR_{20} peptide can easily enter cells (5), we also determined the suitability of applying the PR_{20} peptide to the bath solution (or aCSF). We found that extracellular application of PR_{20} induced hyperexcitability in M1 motor neurons in the presence of synaptic transmission blockers, reaching a steady state usually within 15 min, which was as effective as that seen with intracellular application (*SI Appendix*, Fig. S1 *G* and *H*). To validate the entry of bath-applied PR_{20} into the motor neurons, we used recombinant proteins of green fluorescent protein (GFP)-linked PR_{20} (GFP:PR_{20}). As shown in *SI Appendix*, Fig. S2, 100 nM bath-applied GFP:PR_{20} entered the motor neurons and induced neuronal hyperexcitability indistinguishable from synthetic PR_{20} peptide, while GFP alone did not show any effects. Thus, we used bath application of PR_{20} at the 100-nM level for 20 min to determine the capacity of the PR_{20} peptide to induce increases in intrinsic neuronal excitability in various brain regions in the presence of synaptic blockers.

As demonstrated in Fig. 1 *A* and *B*, in addition to an upward shift in the firing frequency–input current (F-I) curve, L5 motor neurons of M1 also displayed a large reduction in the minimum current required for generating APs (rheobase), a decrease in the threshold potential, and an increase in the input resistance (R_{in}) in response to 100 nM PR_{20} treatment, indicating that PR_{20} increases the intrinsic excitability of motor neurons, possibly by facilitating AP initiation. In contrast, at 100 nM, PR_{20} did not induce hyperexcitability in principal neurons of other brain regions, including L5 PCs of the primary visual cortex (V1) (Fig. 1 *C* and *D*), L5 PCs of the primary somatosensory cortex (S1) (Fig. 1 *E* and *F*), and granule cells (GCs) of the hippocampal dentate gyrus (Fig. 1 *G* and *H*). In hippocampal GCs, PR_{20} rather decreased firing rates at high current injection levels without affecting the resting membrane potential (RMP), rheobase, threshold potential, or R_{in}. Further detailed analysis showed that this reduced excitability was accompanied by a reduction in fast after-hyperpolarization (fAHP) (*SI Appendix*, Fig. S3), implying that reduced after-hyperpolarization may contribute to a PR_{20}-induced decrease in neuronal excitability in hippocampal GCs. As shown in *SI Appendix*, Fig. S4, PCs in layer 3 (L3) of M1 did not respond to 100 nM PR_{20}. Together, these data suggested that the PR_{20} peptide induces hyperexcitability in L5 cortical motor neurons, while principal neurons in V1, S1, and hippocampus are spared from PR_{20}-induced hyperactivation.

As GR poly-dipeptides, encoded by the sense transcript, as well as PR poly-dipeptides, encoded by the antisense transcript, contribute cellular toxicity (5, 6), we sought to examine the effects of synthetic peptide containing 20 repeats of the GR sequence (GR_{20}) on neuronal excitability. Like PR_{20} peptide, an intracellular application of GR_{20} peptide at the 100-nM level induced hyperexcitability in motor neurons, possibly via modulation of AP initiation, while having no effect or inhibitory effect on principal neurons in V1, S1, and hippocampal dentate gyrus (*SI Appendix*, Fig. S5). Together, these data suggest that both PR_{20} and GR_{20} peptides induce hyperexcitability in mouse M1 motor neurons.

PR_{20}-Induced Motor Neuron Hyperexcitability Was Attributable to a Persistent Sodium Current. Next, we sought to investigate the mechanism underlying the PR_{20}-mediated motor neuron hyperexcitability. That PR_{20} peptide application facilitated AP firing in cortical motor neurons suggested that PR_{20} might modulate one of the subthreshold-activating currents that are responsible for the AP threshold and AP initiation. There are four major types of subthreshold currents known in central neurons: the H current (I_h) conducted by hyperpolarization-activated cyclic nucleotide-gated channels,; the small conductance Ca^{2+}-activated K^+ (SK) current conducted by SK channels; the M current (I_M) carried by KCNQ channels; and I_{NaP}, the persistent sodium current conducted by Nav channels (22, 23). To identify which subthreshold-activating current mediated the effect of PR_{20}, we analyzed AP firing in cortical motor neurons following the bath application of PR_{20} in the presence of pharmacological inhibitors of the different subthreshold currents. For this, acute M1 slices were pretreated with each inhibitor individually for 10 min followed by PR_{20} peptide treatment (100 nM, 20 min) while patch-clamp recordings of neuronal activity were undertaken.

Incubation with a specific inhibitor of the SK current (apamin) or I_h current (ZD7288) did not result in any inhibitory effects on PR_{20}-induced changes in AP firing (Fig. 2 *A* and *C*) or biophysical properties of the cells (Fig. 2 *B* and *D*). The KCNQ channel blocker, XE991, prevented an increase in R_{in} (Fig. 2*F*, graph 4). Nevertheless, even in the presence of XE991, PR_{20} treatment effectively increased AP firing with concomitant decreases in the rheobase and threshold potential (Fig. 2 *E* and *F*), similar to that observed with PR_{20} in the

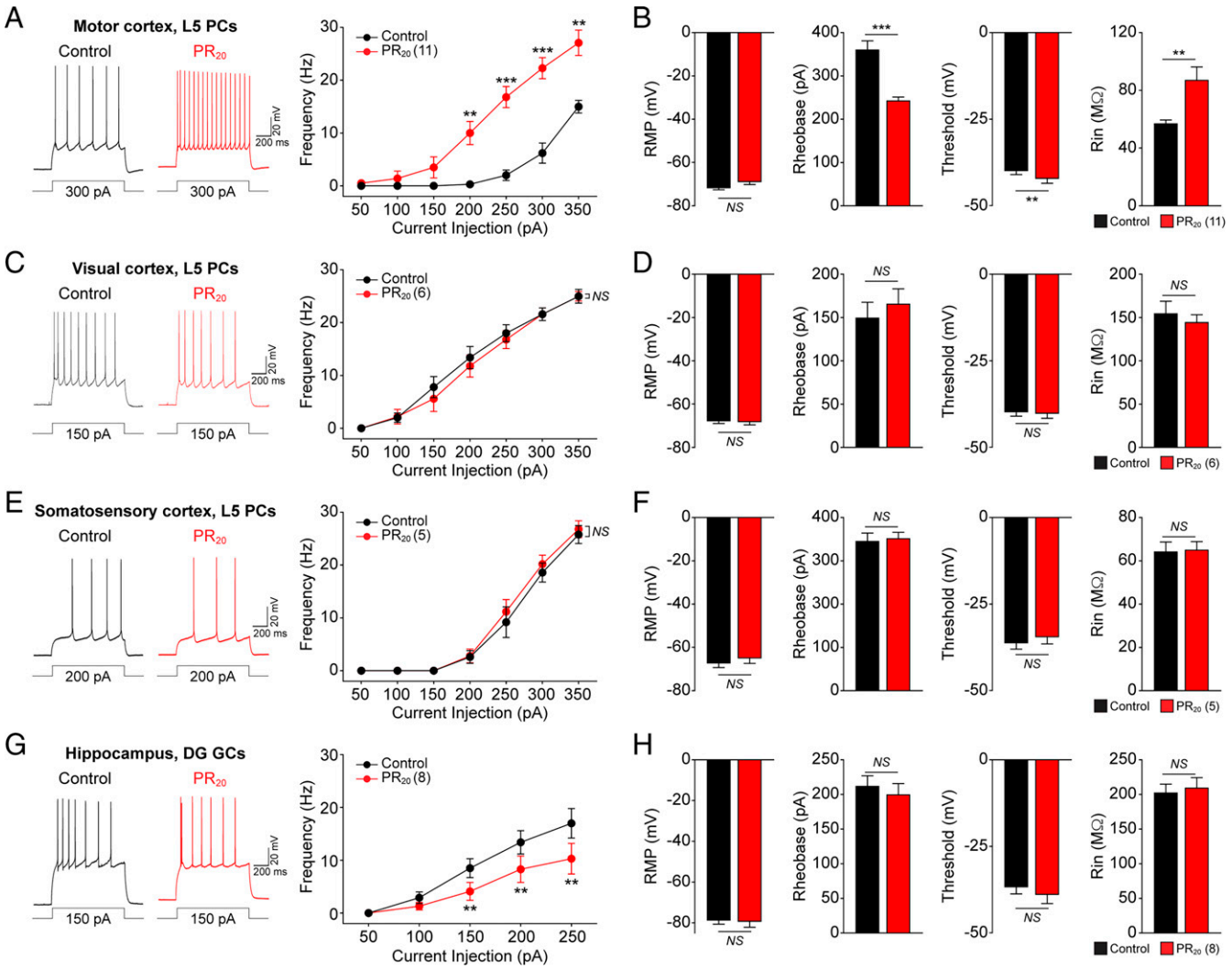

Fig. 1. The PR_{20} poly-dipeptide selectively induces hyperexcitability in cortical motor neurons. Changes in AP firing (*A*, *C*, *E*, and *G*) and intrinsic neuronal biophysical properties (*B*, *D*, *F*, and *H*) of PCs in primary M1 (*A* and *B*; $n = 11$ and 4 mice, respectively), PCs in primary V1 (*C* and *D*; $n = 6$ and 3 mice, respectively), PCs in primary S1 (*E* and *F*; $n = 5$ and 2 mice, respectively), or GCs in hippocampal dentate gyrus (*G* and *H*; $n = 8$ and 2 mice, respectively) were analyzed upon bath application of PR_{20} (100 nM for 20 min). (*A*, *C*, *E*, and *G*) APs were evoked by 1-s depolarizing current steps during current-clamp recordings. (*Left*) Representative traces before (black) and after (red) PR_{20} treatment. (*Right*) Summary plots of the AP frequency vs. injected current (F-I) curve. (*B*, *D*, *F*, and *H*) Summary graphs of RMP, rheobase, threshold potential, and Rin. *NS* indicates not significantly different (paired Student's *t* test). All data are mean ± SEM. $^{**}P < 0.01$; $^{***}P < 0.001$.

absence of XE991 (Fig. 1 *A* and *B*). This indicated that the I_M contributes only minimally to PR_{20}-induced hyperexcitability. In contrast, as shown in Fig. 2 *G* and *H*, the increases in AP firing, decreases in rheobase and threshold potential, and increases in R_{in} induced by PR_{20} were almost completely suppressed when the slices were preincubated for 10 min with a 10-μM concentration of riluzole, a specific I_{NaP} inhibitor (18, 24). Consistent with the notion that these four conductances are active at rest (i.e., at subthreshold potentials), all the inhibitors altered the intrinsic excitability of motor neurons under control conditions. Together, these results indicated that the increased excitability induced by the PR_{20} peptide in cortical motor neurons is largely attributable to an abnormal I_{NaP}.

PR_{20} Specifically Increased I_{NaP} in Cortical Motor Neurons. Having observed that the effect of PR_{20} was blocked by the I_{NaP}-specific inhibitor, we then investigated whether PR_{20} can specifically regulate I_{NaP} in cortical motor neurons. For this, changes in I_{NaP} in cortical motor neurons following bath application of PR_{20} were measured using voltage-clamp recordings, employing Cs^+-based pipette solutions to inhibit K^+ currents. To eliminate synaptic inputs, a mixture of synaptic blockers was added to the bath recording solutions (*Materials and Methods*). As shown in Fig. 3 *A*, *Left*, a slow (60-mV/s) depolarizing voltage ramp from −60 to 0 mV at a holding potential of −70 mV (25, 26) elicited an inward current at the range of I_{NaP} activation under control conditions, starting at potentials slightly lower than −60 mV (the black line). The addition of 100 nM PR_{20} to the control bath solution induced a significant increase in the inward current (the red line in Fig. 3 *A*, *Left*), an effect that was completely blocked by the subsequent application of the sodium channel blocker tetrodotoxin (TTX; 1 μM) (the gray line in Fig. 3 *A*, *Left*), indicating that the inward current recorded using this protocol indeed represented I_{NaP}. Moreover, analysis on TTX-subtracted current traces indicated that PR_{20} treatment clearly increased I_{NaP} magnitude (Fig. 3 *A*, *Right*). Current–voltage (I-V) curves showed that PR_{20} treatment at 100 nM significantly increased the mean I_{NaP} amplitude without altering the shape of the curve (Fig. 3 *B*, *Left*). When analyzed at −20 mV, the average I_{NaP} amplitude was increased from −1.5 ± 0.3 pA/pF (black) to −4.0 ± 0.8 pA/pF (red) with PR_{20} application ($n = 5$, $P < 0.05$) (Fig. 3 *B*,

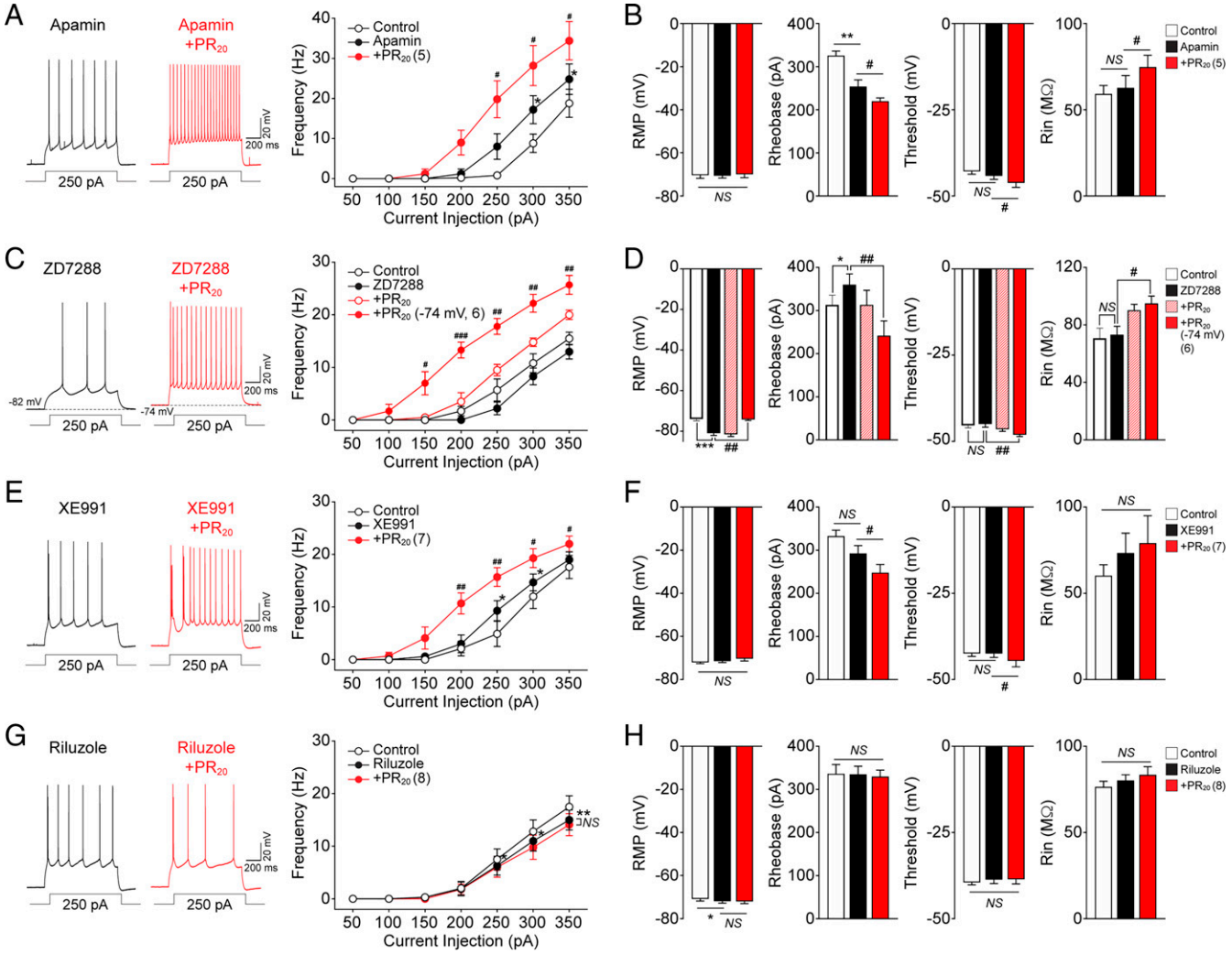

Fig. 2. PR_{20}-induced motor neuron hyperexcitability is attributable to a persistent Na^+ current. Effects of different ion channel blockers on PR_{20}-induced AP firing (*A*, *C*, *E*, and *G*) and intrinsic neuronal biophysical properties (*B*, *D*, *F*, and *H*) in M1 motor neurons preincubated with bath-applied 100 nM apamin (*A* and *B*; $n = 5$ and 2 mice, respectively), 10 μM ZD7288 (*C* and *D*; $n = 6$ and 4 mice, respectively), 50 μM XE991 (*E* and *F*; $n = 7$ and 5 mice, respectively), or 10 μM riluzole (*G* and *H*; $n = 8$ and 3 mice, respectively). In *A*, *C*, *E*, and *G*, *Left* shows representative traces, and *Right* shows averaged F-I curves (from +50 to +350 pA; 1-s, 50-pA increments). White circles indicate control, black circles indicate blocker, and red circles indicate blocker plus PR_{20}. In *C*, AP frequency is shown before (open red circles) and after (closed red circles) the compensation for the ZD7288-induced hyperpolarization. (*B*, *D*, *F*, and *H*) Summary graphs showing changes in RMP, rheobase, threshold potential, and Rin recorded from motor neurons before (white) and after (black) 10 min of pretreatment of chemical blockers and subsequent application of 100 nM PR_{20} (red). *D* shows the values obtained before (striped red) and after (solid red) the cell was held at −74 mV by holding current adjustment during application of ZD7288 + PR_{20}. All data are mean ± SEM. *NS* indicates not significantly different. $^*P < 0.05$ vs. control; $^{**}P < 0.01$ vs. control; $^{\#}P < 0.05$ vs. each channel blocker in the same group (paired Student's *t* test); $^{\#\#}P < 0.01$; $^{\#\#\#}P < 0.001$ vs. each channel blocker in the same group (paired Student's *t* test).

Right). The voltage dependence of activation for I_{NaP} was unaltered ($n = 5$, $P > 0.05$) (Fig. 3*C*). The effects of PR_{20} on I_{NaP} in the motor neuron were further validated by using a step protocol. When the mean residual currents during 480 to 500 ms of the 500-ms voltage steps from −70 to 0 mV from a holding potential of −70 mV were calculated as I_{NaP} (27), 100 nM PR_{20} increased I_{NaP} density without altering resurgent Na^+ currents (*SI Appendix*, Fig. S6). I_{NaP} was corrected for each individual trace by subtracting current recorded in the presence of TTX (1 μM).

That XE991 exerted a suppressive effect on the PR_{20}-induced increase in R_{in} implied that a decrease in I_M contributed to this increase. Given that the PR_{20}-induced increase in R_{in} was also inhibited by riluzole treatment (Fig. 2*H*), it is likely that the PR_{20}-mediated inhibition of I_M might be secondary to the increase in I_{NaP}. To test this idea, we employed whole-cell voltage clamp to isolate I_M using the classical I_M protocol (28) in the presence of Na^+ channel and synaptic blockers but not KCNQ/M channel blockers (*Materials and Methods*). When I_M amplitude was measured as the amplitude of the characteristic slow relaxation (tail current) evoked by a voltage step from –20 to –40 mV, bath application of 100 nM PR_{20} did not alter XE991-sensitive I_M amplitude ($n = 7$, $P > 0.05$) (*SI Appendix*, Fig. S7). These data showed that PR_{20} had no direct effect on I_M, implying that the PR_{20}-mediated inhibition of I_M was a secondary consequence of increasing I_{NaP}. This is consistent with previous studies that Nav and KCNQ/M channels colocalize within the axon initial segment (AIS) and counteract each other to set neuronal excitability (29, 30). Combined, these findings indicated that PR_{20} specifically increases I_{NaP} in cortical motor neurons.

PR_{20}-Induced Hyperexcitability Was Mediated by I_{NaP} Conducted via the Nav1.2-β1-β4 Complex. We then sought to determine the mechanism underlying the PR_{20}-promoted enhancement of I_{NaP} in cortical motor neurons. Navs are multimeric complexes composed of a pore-forming α-subunit and auxiliary β-subunits

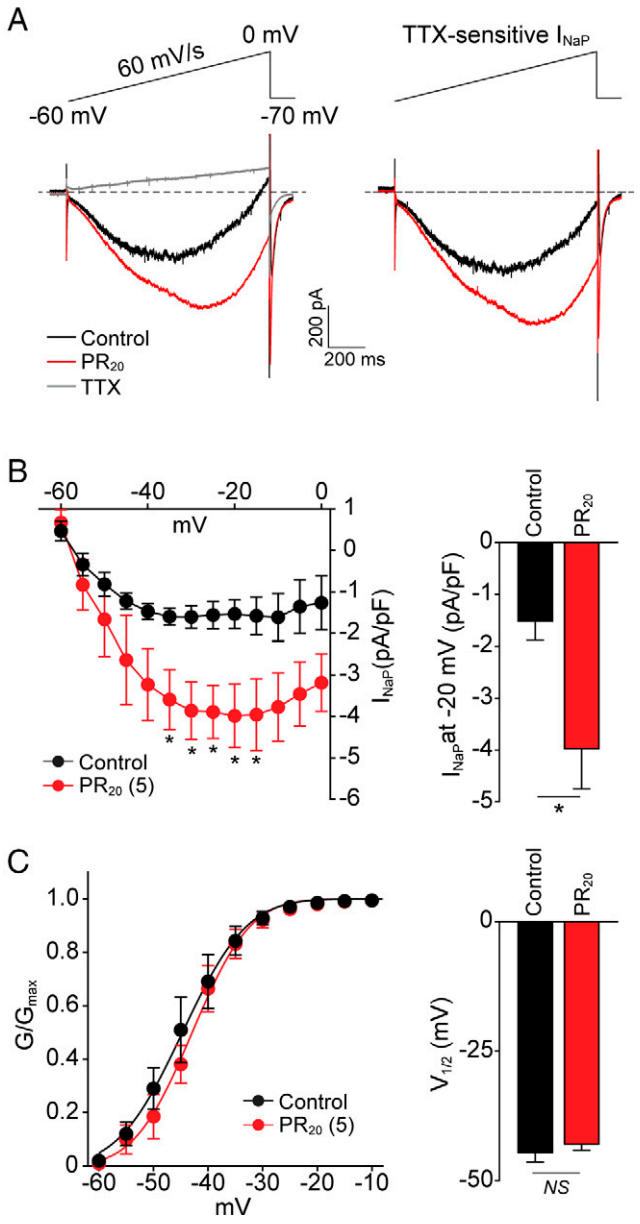

Fig. 3. PR_{20} increases I_{NaP} in cortical motor neurons. (*A*) I_{NaP} evoked by a depolarizing voltage ramp (*Upper*) before (black) and after (red) 10 min of the application of 100 nM PR_{20} followed by 1 μM TTX (gray). TTX-sensitive currents were obtained by subtraction. (*B*) I-V relationships of I_{NaP} (*Left*) and a summary graph at −20 mV (*Right*) before (black) and after (red) PR_{20} application (n = 5 and 3 mice, respectively). (*C*) Steady-state activation curves of I_{NaP} (*Left*) and summary for half-activation voltage $V_{1/2}$ (*Right*) before (black) and after (red) PR_{20} application (n = 5 and 3 mice, respectively). All data are mean ± SEM. *NS* indicates not significantly different. *P < 0.05 (paired Student's t test). pA, pico ampere; pF, picofarad.

(31, 32). Nav1.2 and Nav1.6 are two predominant forms of the nine known mammalian α-subunits in excitatory pyramidal neurons in the cerebral cortex and may cooperate in the initiation and propagation of APs (33). In the mammalian brain, the β1-, β2-, and β4-subunits predominate in postnatal development, showing distinct spatiotemporal expression patterns, whereas β3 is highly expressed during embryonic development (32, 34). In the previous studies, antibodies specifically targeting ion channels have been used as channel blockers and developed as potential therapeutics in neurological diseases as well as cancer (35–37). Thus, to identify the Nav isoforms responsible for PR-induced hyperexcitability in motor neurons, we microinjected antibodies targeting each isoform into motor neurons using intracellular perfusion through a patch pipette. After patch break-in, 15 min was allowed for dialysis of the Nav antibodies, and then, PR_{20} was bath applied. Series resistance (Rs) was monitored during the recording, and cells were discarded when the Rs had changed by >20% compared with the baseline value. Rabbit immunoglobulin G (IgG) was used as a negative control for the ability of Nav antibodies to block the effects of the PR_{20} peptide and was applied to motor neurons at the same concentration as that used for the Nav antibodies (0.4 μg/mL). In the presence of control IgG, PR_{20} increased I_{NaP} density at −20 mV by 127.9 ± 37.2% (n = 5) (Fig. 4*A*), which was indistinguishable from that in cells without IgG (155.5 ± 48%, n = 5, P > 0.05). We observed that a PR_{20}-induced increase in I_{NaP} was blocked by anti-Nav1.2 antibodies (−12.2 ± 14.4%, n = 7, P < 0.01 vs. IgG) but not anti-Nav1.6 antibodies (73.2 ± 33.1%, n = 5, P > 0.05 vs. IgG) (Fig. 4*A*). We also individually applied anti-β1, -β2, and -β4 antibodies through a patch pipette. Antibodies against β1 or β4 effectively suppressed PR_{20}-induced increases in I_{NaP} (β1: 2.7 ± 4.8%, n = 5, P < 0.05 vs. IgG; β4: −1.6 ± 12.0%, n = 6, P < 0.01 vs. IgG), whereas anti-β2 antibodies did not (73.0 ± 19.3%, n = 3, P > 0.05 vs. IgG) (Fig. 4*A*). These data suggested that the antibodies against Nav1.2, β1, and β4 specifically interfered with the PR_{20}-mediated effects on I_{NaP} in cortical motor neurons. We confirmed that all the antibodies tested were specific to the given Nav subunits (*SI Appendix*, Fig. S8).

To examine whether anti-Nav antibodies can also block PR_{20}-induced hyperexcitability, we delivered Nav-targeting antibodies into motor neurons as described above. In the presence of control IgG, PR_{20} effectively induced hyperexcitability with concomitant changes in the biophysical properties of the neurons, similar to that observed in cells treated with PR_{20} only (Fig. 4*B* and *SI Appendix*, Fig. S9*A*). As shown in Fig. 4 *C–G* and *SI Appendix*, Fig. S9 *B–F*, antibodies against Nav1.2, β1, or β4, but not Nav1.6 or β2, prevented PR_{20}-induced increases in firing rates and all the PR_{20}-induced changes in biophysical properties. These data showed a pattern of significant concordance between the ability of anti-Nav antibodies to block PR_{20}-induced I_{NaP} and their ability to block PR_{20}-induced hyperexcitability, indicating that anti-Nav1.2, -β1, and -β4 antibodies inhibited hyperexcitability by blocking I_{NaP}. Of note, all the anti-Nav antibodies tested here did not affect AP firing of motor neurons under control condition (*SI Appendix*, Fig. S10), which is consistent with previous observations that antibodies targeting intracellular segments between domains I and II or II and III of Nav α-subunit do not interrupt channel function recorded by the patch-clamp technique (38, 39). Given that one α-subunit is generally associated with two β-subunits in vivo, one through a noncovalent bond (β1 or β3) and the other via a covalent bond (β2 or β4) (31, 32), these data suggested a possibility that PR might induce hyperexcitability by modulating an Nav1.2-β1-β4 complex in cortical motor neurons.

β4 Was Critical for the PR_{20}-Mediated Modulation of Nav1.2 Channels. To further test this hypothesis, we performed reconstitution assays in HEK-293T cells using two of the human α-subunits (hNav1.2 and hNav1.6) and three of the human β-subunits (hβ1, hβ2, and hβ4). We first determined the effects of the PR_{20} peptide on hNa1.2 channels coexpressed with a combination of either Discosoma red (DsRed)-linked hβ1 (hβ1:DsRed) and GFP-linked hβ2 (hβ2:GFP) or hβ1:DsRed and GFP-linked hβ4 (hβ4:GFP). We found that PR_{20} did not affect the channel activity of hNav1.2 α-subunits alone or the

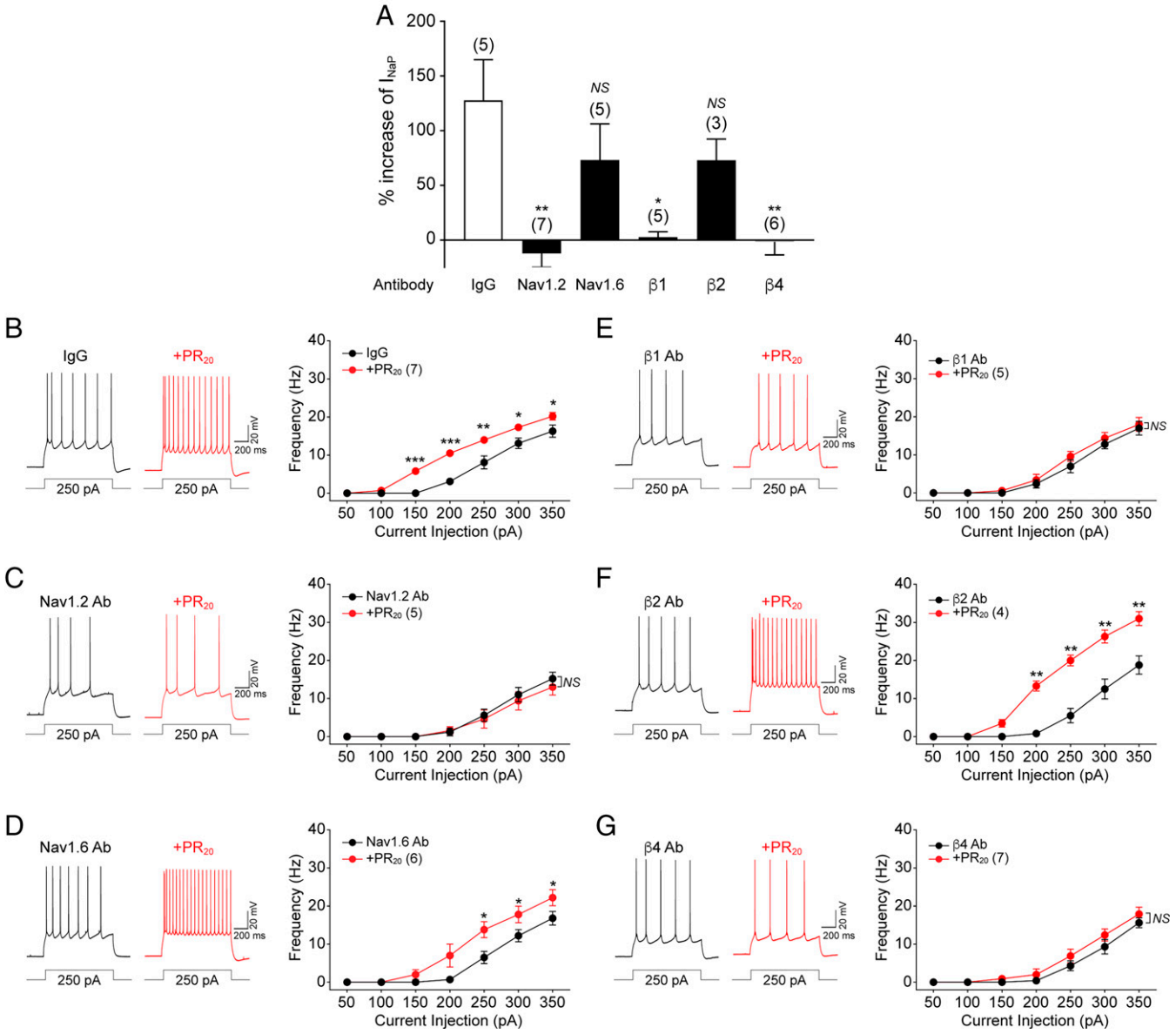

Fig. 4. Both I_{NaP} and hyperexcitability induced by PR_{20} are blocked by antibodies targeting Nav1.2, β1, and β4. (*A*) A percentage increase graph for changes in I_{NaP} at −20 mV of cortical motor neurons by PR_{20} treatment (100 nM, 20 min) in the presence of the control IgG or Nav antibodies as indicated. I_{NaP} was evoked by a depolarizing voltage ramp (−60 to 0 mV, 60 mV/s). All data are mean ± SEM. IgG: $n = 5$ and 2 mice. Nav1.2: $n = 7$ and 4 mice. Nav1.6: $n = 5$ and 2 mice. β1: $n = 5$ and 2 mice. β2: $n = 3$ and 2 mice. β4: $n = 6$ and 3 mice. Numbers of cells/mice analyzed are shown in parentheses. *NS* indicates not significantly different. $^*P < 0.05$ vs. cells with control IgG (Student's *t* test); $^{**}P < 0.01$ vs. cells with control IgG (Student's *t* test). (*B–G*) Effects PR_{20} on AP firing in IgG-injected (*B*; $n = 7$ and 2 mice), anti-Nav1.2 antibody–injected (*C*; $n = 5$ and 2 mice), anti-Nav1.6 antibody–injected (*D*; $n = 6$ and 2 mice), anti-β1 antibody–injected (*E*; $n = 5$ and 3 mice), anti-β2 antibody–injected (*F*; $n = 4$ and 2 mice), and anti-β4 antibody–injected (*G*; $n = 7$ and 3 mice) motor neurons. (*Left*) Representative AP traces in response to 250-pA current injection (1-s duration) before (black) and after (red) PR_{20} treatment (100 nM, 20 min). (Right) Averaged F-I curve (from +50 to +350 pA; 1-s, 50-pA increments) before (black) and after (red) PR_{20} treatment (100 nM, 20 min). All data are mean ± SEM. $^*P < 0.05$ vs. before PR_{20} treatment in the same group (paired Student's *t* test); $^{**}P < 0.01$ vs. before PR_{20} treatment in the same group (paired Student's *t* test); $^{***}P < 0.001$ vs. before PR_{20} treatment in the same group (paired Student's *t* test).

hNa1.2 in the presence of hβ1:DsRed and hβ2:GFP, as observed in the I-V relationship and the steady-state activation relationship (Fig. 5*A*, Table 1, and *SI Appendix*, Fig. S11 *A–C*). When hβ1:DsRed and hβ4:GFP were present, however, PR_{20} administration significantly increased hNav1.2 channel activity with a left shift in the activation curve (Fig. 5*B*, Table 1, and *SI Appendix*, Fig. S11*D*). In contrast, PR_{20} treatment did not affect Nav1.6 channel activity in the presence of either β-subunit combination (Fig. 5 *C* and *D*, Table 1, and *SI Appendix*, Fig. S11 *E* and *F*). These results were consistent with the idea that the Nav1.2-β1-β4 complex mediates the effects of PR_{20}. In further dissecting the role of β-subunits in mediating PR_{20} effects, each of the three β-subunits was coexpressed with hNav1.2, and the transfected cells were subjected to the voltage-clamp recording upon PR_{20} application. As shown in Fig. 5 *E–G*, coexpression of hβ4:GFP alone was enough for hNav1.2 to be aberrantly modulated by PR_{20}, while hNav1.2 channel activity was not increased by PR_{20} when coexpressed with either the hβ1:GFP or hβ2:GFP subunit. The voltage dependence of steady-state activation for each condition is analyzed in Table 1 and *SI Appendix*, Fig. S11 *G–I*.

A previous study has shown that substitution of the cysteine 58 of hβ4, which is required for forming a disulfide bond with C910 in the Nav1.2 channel, to alanine (C58A) disrupts the pharmacological properties of Nav1.2 without affecting the folding or membrane trafficking of the protein (40). Thus, to

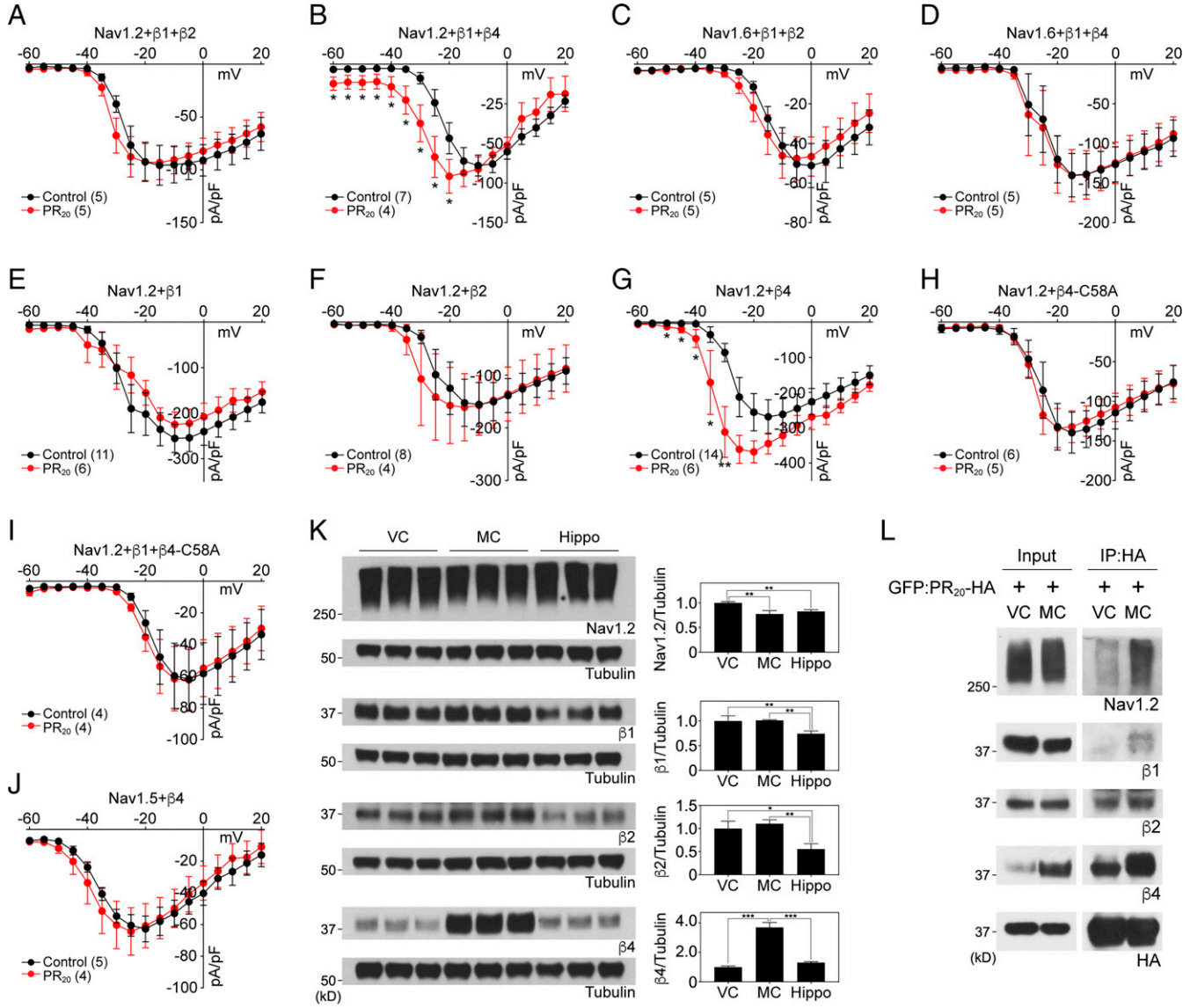

Fig. 5. β4 is critical for the PR_{20}-mediated modulation of Nav1.2 channels. (*A–J*) Effects of PR_{20} peptide on I-V relationships of the hNav1.2 channel coexpressed with β1 and β2 (*A*), the hNav1.2 channel coexpressed with β1 and β4 (*B*), the hNav1.6 channel coexpressed with β1 and β2 (*C*), the hNav1.6 channel coexpressed with β1 and β4 (*D*), the hNav1.2 channel coexpressed with β1 (*E*), the hNav1.2 channel coexpressed with β2 (*F*), the hNav1.2 channel coexpressed with β4 (*G*), the hNav1.2 channel coexpressed with the β4 C58A mutant (*H*), the hNav1.2 channel coexpressed with the β1 and β4 C58A mutant (*I*), and the hNav1.5 channel coexpressed with β4 (*J*) in HEK-293T cells. Currents were elicited from a V_h of −120 mV to test potentials ranging from −60 to +20 mV in 5-mV increments. Black circles indicate control; red circles indicate 150 s after PR_{20} application. All data are mean ± SEM. $^*P < 0.05$ vs. control in the same group (Student's *t* test); $^{**}P < 0.01$ vs. control in the same group (Student's *t* test). (*K*) Western blotting images showing the expression profiles of Nav1.2, β1, β2, and β4 in V1, M1, or hippocampus. Quantification of the band intensity was performed using ImageJ (NIH). One-way ANOVA was used to evaluate statistical significance. $^*P < 0.05$; $^{**}P < 0.01$; $^{***}P < 0.001$. (*L*) Interactions between bath-applied GFP-linked PR_{20} with a C-terminal HA tag (GFP:PR_{20}-HA) and Nav subunits (Nav1.2, β1, β2, and β4) in visual or motor cortices were assessed by pull-down assay using HA magnetic beads. Hippo, hippocampus; MC, M1; VC, V1; HA, hemagglutinin; IP; immunoprecipitation; pA, pico ampere; pF, picofarad.

assess whether the coupling of hβ4 to hNav1.2 is critical for Nav1.2 sensitivity to PR_{20}, we analyzed the effect of PR_{20} on hNav1.2 in the presence of hβ4-C58A linked to GFP (hβ4-C58A:GFP). As shown in Fig. 5 *H* and *I*, PR_{20} failed to increase the activity of the hNav1.2 channel coexpressed with hβ4-C58A:GFP alone (Fig. 5*H*) or hβ4-C58A:GFP together with hβ1:DsRed (Fig. 5*I*), suggesting that the β4-subunit plays a key role in the PR_{20}-mediated modulation of Nav1.2. The voltage dependence of steady-state activation for each condition is analyzed in Table 1 and *SI Appendix*, Fig. S11 *J* and *K*. The β4-subunit is also highly expressed in the heart where Nav1.5 is the major α-subunit (34). However, the activity of hNav1.5 coexpressed with hβ4:GFP in HEK-293T cells was not modulated by PR_{20} application (Fig. 5*J*, Table 1, and *SI Appendix*, Fig. S11*L*). Even though the motor neuron excitability was assessed in the presence of the synaptic blockers to prevent the input from other cells, including the interneurons, we further examined the effects of PR_{20} peptide on Nav1.1, a major sodium channel in interneurons (41). As shown in *SI Appendix*, Fig. S12, the activity of hNav1.1 coexpressed with or without hβ4:GFP in HEK-293T cells was unaffected by PR_{20} application. Together, these data suggest that the effect of PR_{20} is specific to neuronal subtype, Nav1.2 in combination with β4.

Supporting these observations, western blotting analysis across brain regions revealed that β4 exhibited a more than threefold higher expression profile in M1 than in V1 or hippocampus (Fig. 5*K*). Nav1.2 expression was slightly lower in M1 and hippocampus than in V1. Expression levels of β1 and β2

Table 1. Parameters obtained from steady-state activation curve fittings with Boltzmann function

	Control		PR_{20}	
	$V_{1/2}$ (mV)	*k*	$V_{1/2}$ (mV)	*k*
Nav1.2 + β1+ β2	−22.6 ± 3.4 (*n* = 5)	5.4 ± 0.5	−23.2 ± 2.4	6.6 ± 0.5
Nav1.2 + β1+ β4	−17.8 ± 3.2 (*n* = 4)	6.0 ± 1.4	−28.0 ± 2.1*	4.6 ± 0.6
Nav1.6 + β1+ β2	−11.3 ± 0.7 (*n* = 5)	5.0 ± 0.4	−13.6 ± 2.6	5.4 ± 0.7
Nav1.6 + β1+ β4	−19.9 ± 2.0 (*n* = 5)	6.0 ± 0.9	−21.1 ± 2.4	6.1 ± 1.3
Nav1.2 + β1	−21.7 ± 3.4 (*n* = 6)	3.5 ± 0.6	−23.6 ± 2.8	3.2 ± 0.4
Nav1.2 + β2	−21.4 ± 3.3 (*n* = 4)	4.3 ± 0.9	−23.4 ± 4.0	3.6 ± 1.0
Nav1.2 + β4	−27.5 ± 0.3 (*n* = 6)	2.6 ± 0.4	−34.2 ± 1.1**	2.7 ± 0.6
Nav1.2 + β4 C58A	−25.8 ± 2.2 (*n* = 5)	3.7 ± 0.5	−27.6 ± 1.5	3.4 ± 0.7
Nav1.2 + β1 + β4 C58A	−13.5 ± 1.8 (*n* = 4)	6.3 ± 1.5	−16.5 ± 1.8	6.4 ± 1.5
Nav1.5 + β4	−36.3 ± 1.9 (*n* = 4)	6.2 ± 0.5	−37.8 ± 2.7	4.9 ± 0.3
Nav1.2	−13.4 ± 0.5	6.1 ± 0.4	−15.4 ± 0.6	7.7 ± 0.5
Nav1.1	−11.3 ± 0.5	7.3 ± 0.5	−13.9 ± 0.4	7.2 ± 0.5
Nav1.1+ β4	−19.1 ± 0.4	5.5 ± 0.3	−21.9 ± 0.4	5.5 ± 0.4

Asterisks indicate values derived from fitting the Boltzmann function that differ from the corresponding values in control condition. *$P < 0.05$, paired Student's *t* test; **$P < 0.01$, paired Student's *t* test.

were lower in hippocampus compared with visual and motor cortices. Moreover, in a pull-down assay using GFP:PR_{20}, the interaction between Nav1.2 and GFP:PR_{20} was stronger in the M1 where β4 expression is higher than in the V1 (Fig. 5*L*). The β1-subunit, which is evenly expressed in visual and motor cortices, also coprecipitated with GFP:PR_{20} more strongly in the M1 (Fig. 5*L*). The β2- or β4-subunits exhibited coprecipitation profiles proportional to their expression levels in two brain regions (Fig. 5*L*). Thus, these data suggest the possibility that β4 plays a pivotal role in PR_{20} poly-dipeptide–induced I_{NaP} via an Nav1.2 channel complex, resulting in selective hyperexcitability in cortical motor neurons.

Discussion

In this study, we present evidence that PR poly-dipeptides resulting from RAN translation of *C9orf72*-associated repeat expansions cause hyperexcitability in cortical motor neurons. By recording the functions of various types of neurons in the mouse brain, we showed that treatment with PR_{20} peptides dose dependently increased the intrinsic excitability of motor neurons in the M1 but not that of principal neurons in the V1, S1, or hippocampus (Fig. 1). Electrophysiological analysis of brain slices using ion channel–specific inhibitors revealed that PR_{20}-induced motor neuron hyperexcitability was principally mediated by an aberrant increase in I_{NaP} (Figs. 2 and 3). Using isoform-specific Nav antibodies, we showed that both I_{NaP} and hyperexcitability induced by PR_{20} could be blocked by antibodies targeting Nav1.2, β1, and β4, implying that an Nav1.2-β1-β4 complex might mediate the PR_{20}-induced I_{NaP} in motor neurons (Fig. 4). Through heterologous expression of neuronal sodium channels in HEK-293T cells, combined with mutational analysis, we established that PR_{20} regulated the Nav1.2-β1-β4 complex and that the auxiliary β4-subunit was critical for the PR_{20}-mediated modulatory effect (Fig. 5). Additionally, we found that β4 expression was higher in the M1 than in the V1 or the hippocampus, which is an intriguing finding given that distinct β-subunit expression patterns might underly tissue-dependent variations in Nav-channel pharmacological properties (40). Indeed, we observed that PR_{20} more avidly bound Nav1.2 in the M1 than the V1 (Fig. 5). Together, these data suggested that PR poly-dipeptides increase I_{NaP} possibly through the modulation of an Nav1.2-β1-β4 complex, which in turn, facilitates AP initiation and increases neuronal excitability in cortical motor neurons.

Cortical hyperexcitability can be caused by altered synaptic properties as well as enhanced intrinsic excitability (20). Evidence supporting the role of synaptic properties in cortical hyperexcitability has been provided in the previous studies where rodents harboring mutations in two ALS-associated genes, *SOD1* and *TDP-43*, exhibit hypoactivity in inhibitory interneurons (42–45). Changes in intrinsic excitability relate to alterations in the functional properties of dendritic and somatic voltage- and Ca^{2+}-gated ion channels (46). Surprisingly, we found that the PR poly-dipeptides specifically regulate I_{NaP} in cortical motor neurons, establishing a causal link between *C9orf72* repeat expansion and the intrinsic excitability of cortical motor neurons in *C9orf72* ALS. Consequently, our findings indicate that diverse pathways may be involved in inducing cortical hyperexcitability. Although PR_{20} peptide did not modulate the channel activity of Nav1.1 coexpressed with β4 in HEK-293T cells, it is still possible that *C9orf72* poly-dipeptides can act on inhibitory interneurons or astrocytes to further exacerbate motor neuron hyperexcitability. This possibility should be examined in future studies.

The β-subunits are known to play a key role in shaping the overall pharmacological sensitivities of the Nav channel signaling complex (40). Several potential principles underlying β-subunit modulation of Nav1.2 channel pharmacology have been proposed. First, ligands may directly bind to β-subunits (47), an intriguing concept that has also been observed with the voltage-gated Ca^{2+} channel inhibitor gabapentin, which acts through the transmembrane α2δ-subunit (48). Alternatively, toxic proteins may only bind to Nav1.2 in a particular conformational state that is induced by β-subunits. This hypothesis was suggested by the previous studies that disrupting β4-interaction with Nav1.2 by introducing a β4-C58A mutation changes a conformation of the Nav1.2-β4 complex, in turn altering its toxin sensitivity (40, 49). Our results showed that β4 coexpression confers PR_{20} sensitivity to Nav1.2 but not to Nav1.5 or Nav1.6 α-subunits, and a sensitivity of Nav1.2 to PR_{20} is lost when wild-type β4 was replaced with the C58A mutant. Thus, it is plausible that β4 might determine a particular conformation of Nav1.2 and thereby, expose binding sites for PR_{20}. We also observed that antibodies preventing PR_{20} induced I_{NaP} in motor neuron targets Nav1.2, β1, and β4,

which are the same Nav complex subunits required for the reconstitution of PR_{20} sensitivity in HEK-293T cells (Figs. 4 and 5). These observations suggest the possibility that these antibodies may interfere with PR_{20}-mediated modulation of Nav1.2 by changing conformation of the Nav1.2-β1-β4 complex rather than sequestering the PR_{20} peptide.

In the central nervous system, heteromeric KCNQ2/3 potassium channels generate the I_M, a subthreshold potassium current (50, 51). Due to slow gating kinetics, the I_M effectively counters sustained membrane depolarization and repetitive AP firing (52). Thus, KCNQ/M channel impairment through loss of function mutations or pharmacological inhibition leads to neuronal hyperexcitability (50, 53). Here, we showed that the I_M blocker XE991 prevented PR-induced increases in R_{in}. However, the PR-mediated modulation of the I_M appeared to be exerted indirectly through I_{NaP} enhancement (*SI Appendix*, Fig. S7). The interrelatedness of I_{NaP} and K^+ channels represents a well-known means through which neurons can tune their excitability (29, 54). In rat mitral cells of the olfactory bulb, gamma-Aminobutyric acid-B (GABA-B) receptor activation modulates the I_{NaP}, and I_{NaP}, in turn, inhibits the sodium-activated potassium current that is coupled to it. Similarly, in interneurons of the locomotor central pattern generator region, I_M modulation adjusts I_{NaP} amplitude (30). Our data add support to the notion of the interplay between these two currents.

PR_{20} and GR_{20} showed minimal effects on principal neurons of the visual and somatosensory cortices but decreased the intrinsic excitability of hippocampal dentate gyrus GCs (Fig. 1 and *SI Appendix*, Fig. S5). This is consistent with observations that the visual and somatosensory cortices are only minimally affected in ALS patients, while up to 50% of ALS patients have some degree of cognitive or behavioral impairment (55, 56). Frontotemporal dementia (FTD) is a now well-established component of ALS (57), underscoring that this disorder forms part of a spectrum of central neurodegenerative processes. Indeed, the hexanucleotide repeat expansion in *C9orf72* is the most common cause of both FTD and ALS, supporting their shared origins (58). We also found that reduced excitability in PR_{20}-treated hippocampal neurons is accompanied by a decrease in fAHP (*SI Appendix*, Fig. S3). Since fAHP is mediated by several voltage-gated K^+ channels (59, 60), our observations imply that PR_{20} might decrease neuronal excitability via K^+ channels in hippocampal neurons. Further studies are needed to identify the detailed mechanisms.

Here, we identify the PR poly-dipeptides–mediated enhancement of I_{NaP} as a key mechanism for the hyperactivity of motor neurons in *C9orf72* ALS. In terms of disease progression for ALS patients carrying *C9orf72* repeat expansion, M1 hyperexcitability begins long before the onset of motor symptoms (16, 20). Effects of poly-dipeptides on cellular function and cell viability have normally been driven by exposing cells to high extracellular levels of poly-dipeptides (5, 61), which may be more relevant to late stages of ALS. In contrast, we characterized the rapid effects of PR_{20} poly-dipeptides on the activity of cortical motor neurons at nanomolar concentrations, substantially lower than those used in previous studies. We also showed that the neuronal activity of L3 PCs in M1 was not affected by 100 nM PR_{20} peptide, reminiscent of the clinical observations that L3 PCs are spared in the early stages of ALS with their loss seen in more advanced stages (62). Thus, we speculate that RAN translation of the hexanucleotide repeats may take place at very low levels in presymptomatic decades, which are enough to hyperactivate cortical motor neurons but not sufficient to impair other cellular functions, such as RNA biogenesis or nucleolar dysfunction. As *C9orf72* repeats can go on to produce poly-dipeptides, the expression of PR poly-dipeptides is finally sufficient to begin to impede splicing of the *EAAT2* transcripts in astrocytes. This impediment might decrease the reuptake of excess glutamate released by hyperactivated motor neurons, favoring accumulation of glutamate in the synaptic cleft, which in turn, leads to glutamate excitotoxicity and eventually, to the selective neurodegeneration of lower motor neurons in *C9orf72* ALS. By elucidating the molecular mechanisms of cortical hyperexcitability in the early stages, our study improves our understanding of *C9orf72* ALS and provides a basis for presymptomatic intervention that may alter the course of disease.

Materials and Methods

Synthesis of PR_{20} and GR_{20} Peptides. Peptides containing 20 repeats of PR or GR with an HA tag at its C terminus were synthesized from the Protein Chemistry Core at the University of Texas Southwestern Medical Center. Peptides were synthesized on an Applied Biosystems 433 automated peptide synthesizer using optimized fluorenylmethoxycarbonyl (Fmoc) chemistry as described elsewhere (63). Crude peptides were purified on a Waters 600 high-performance liquid chromatography (HPLC) system using a Vydac C18 semipreparative column (25 × 10 mm) at 3 mL/min and 0 to 100% B in 120 min, where A is water/0.045% trifluoroacetic acid (TFA) and B is acetonitrile/0.036% TFA. The purified peptides were characterized using electrospray ionization mass spectroscopy (ESI-MS).

Preparation of Acute Brain Slices. Brain slices were prepared from 8-wk-old male mice (C57BL/6N). Animals were housed three to five mice per cage and maintained with food and water freely available. Mice were euthanized with rapid decapitation after carbon dioxide exposure. The brain was immediately removed from the skull and immersed in ice-cold oxygenated slicing solution (220 mM sucrose, 26 mM $NaHCO_3$, 2.5 mM KCl, 1 mM NaH_2PO_4, 5 mM $MgCl_2$, 1 mM $CaCl_2$, 10 mM D-glucose, pH 7.35 to 7.4) saturated with 95% O_2/5% CO_2. The brain tissue blocks were transected transversely to produce coronal slices using a vibratome (VT1200S; Leica) with a thickness of 100 μm for immunohistochemistry, 200 μm for immunoprecipitation, or 320 μm for whole-cell patch-clamp recordings. Slices were then transferred to a homemade holding chamber and incubated at 34 °C for 30 min, and they were thereafter maintained at room temperature until in situ slice patch-clamp recordings.

Whole-Cell Patch-Clamp Recording. Cells in slices were visually identified based on their size, shape, and location using an upright microscope equipped with differential interference contrast optics (BX51WI; Olympus). Whole-cell recordings were obtained with a Multiclamp 700B amplifier (Molecular Devices) and pClamp 10.6 software (Axon Instruments, Inc.). The patch pipettes were pulled from borosilicate capillaries (Hilgenberg GmbH) using a Narishige puller (PC-10; Narishige). The patch pipettes had a resistance of 3 to 5 MΩ when filled with pipette solution (130 mM K-gluconate, 10 mM KCl, 10 mM Hepes (4-(2-hydroxyethyl)-1-piperazineethanesulfonic acid), 4 mM MgATP (adenosine triphosphate magnesium salt), 0.3 mM NaGTP (guanosine triphosphate sodium salt), 10 mM Na_2-Phosphocreatine, pH 7.3). The bath solution (126 mM NaCl, 26 mM $NaHCO_3$, 2.8 mM KCl, 1.25 mM NaH_2PO_4, 2.5 mM $CaCl_2$, 1.2 mM $MgSO_4$, 20 mM glucose, pH 7.4) was saturated with carbogen (95% O_2 and 5% CO_2). The perfusion rate of the bathing solution and the volume of the recording chamber for the slices were 1.7 ml/min and 2 to 2.3 ml, respectively. The Rs after establishing the whole-cell configuration was between 10 and 15 MΩ. The experiments were performed at 32 °C ± 1 °C.

For current-clamp experiments to analyze neuronal excitability, D-2-amino-5-phosphonopentanoate (D-AP5, 50 μM), 6-cyano-2,3-dihydroxy-7-nitro-quinoxaline (CNQX, 10 μM), and SR-95531 (gabazine, 20 μM) were included in bath solutions to block all excitatory (α-amino-3-hydroxy-5-methyl-4-isoxazolepropionic acid (AMPA) and N-methyl-D-aspartate (NMDA) receptors) and inhibitory (gamma-Aminobutyric acid-A (GABA-A) receptors) synaptic inputs. APs were evoked by increasing current injections (from +50 to +350 pA; 1-s, 50-pA increments). The following parameters were measured: 1) the RMP, 2) the AP rheobase (current threshold for single AP generation, 30-ms duration), 3) the AP threshold potential, 4) R_{in} (membrane potential changes [V] for a given hyperpolarizing current [50-pA, 500-ms] input), and 5) the F-I curve (firing frequencies against the amplitude of the injected currents; from +50 to +350 pA). To

compensate for the ZD 7288–induced hyperpolarization, the membrane potential was held at −74 mV by continuous adjustment of the holding current. In primary M1, we identified interneurons with distinct electrophysiological and morphological characteristics (64).

For voltage-clamp experiments to analyze I_{NaP}, $CdCl_2$ (0.2 mM) and 4-Aminopyridine (4-AP; 5 mM) were additionally applied to block Ca^{2+} and outward K^+ currents, respectively. I_{NaP} was recorded in the same bath solution as current-clamp recording and a pipette solution (130 mM Cs-Methanesulfornate, 10 mM CsCl, 10 mM Hepes, 4 mM MgATP, 0.3 mM NaGTP, 5 mM Na_2-Phosphocreatine, 5 mM ethylene glycol-bis(beta-aminoethyl ether)-N,N,N',N'-tetraacetic acid (EGTA), 10 mM Tetraethylammonium chloride (TEA-Cl), pH 7.3). Under these conditions and using a ramp stimulus protocol (−60 to +0 mV, 60 mV/s) from a holding potential of −70 mV to evoked I_{NaP}, we could record I_{NaP} without any AP currents out of voltage-clamp control. After recording currents in the control condition, we added TTX (1 μM) sequentially for pharmacological dissection of voltage-gated Na^+ current. In the presence of TTX, the ramp protocols evoked only a small outward current, which activated at more positive membrane potentials than I_{NaP} (Fig. 3 *A*, *Left*). The difference currents between inward Na^+ currents in control and in TTX were regarded as TTX-sensitive currents. I-V curves for I_{NaP} were constructed from the ramp-evoked I_{NaP} (mean current value over 0.01-mV intervals from averages of four to five trials for each cell to approximate quasisteady-state current). In order to confirm the PR_{20} effects on I_{NaP} in motor neurons, we also evoked I_{NaP} by the 500-ms voltage steps from −70 to 0 mV from a holding potential of −70 mV. I_{NaP} was measured as the preserved currents from 480 to 500 ms after stimulus. I_{NaP} was corrected for each individual trace by subtracting the current recorded in the presence of TTX (1 μM). To reduce voltage errors, Rs was compensated by ∼70 to 90% when recording sodium currents. Currents were normalized to corresponding cell capacitance for better comparison. Steady-state activation data were fitted by Boltzmann function. Recordings of I_M in motor neurons were performed in the presence of Na^+ blocker (0.5 μM TTX) and synaptic blockers (50 μM D-AP5, 10 μM CNQX, and 20 μM SR-95531). Neurons were held at −20 mV to activate the I_M before a deactivation step at −40 mV for 1 s for the current relaxation to record the native I_M.

Plasmids and Cloning. Plasmid DNA for human SCN2A (hNav1.2) expression (pcDNA3.1-DYK-Nav1.2) was purchased from GenScript. Plasmid DNA for human SCN8A (hNav1.6) expression (pCMV6-AC-Myc-DDK) was purchased from ORIGENE. Plasmid DNA for human SCN1A (hNav1.1) was purchased from Genecopoeia. To generate expression constructs for Nav β, DNA fragments encoding SCN1B (β1), SCN2B (β2), and SCN4B (β4) were amplified by PCR using Human Brain, Cerebral Cortex QUICK-Clone cDNA (Clontech) as a template. The amplified fragments were then subcloned into GFP-N1 or DsRed-N1 vectors (Clontech) to generate GFP- or DsRed-linked fusion gene constructs for β-subunits. The SCN5A plasmid was provided by Gordon F. Tomaselli.

The plasmids for Nav1.2 and Nav1.6 were prepared as described earlier (65). Briefly, 20 ng of plasmid DNA was transformed into 50 μL of Stbl3 competent cells and kept on ice for 25 min. The cells were then heat shocked at 42 °C for 40 s and incubated for 2 min on ice. Upon addition of 450 μL Super Optimal broth with Catabolite repression (SOC) medium, cells were incubated at 30 °C for 90 min. Then, 50 μL of the cells were plated onto an Luria-Bertani^{Amp+} (LB^{Amp+}) agar plate and incubate at 30 °C for 3 to 5 d until two distinct populations (large fast-growth colonies and small slow-growth colonies) appeared. Several small colonies were inoculated into LB^{Amp} broth and grown for 2 to 3 d at 30 °C. The plasmids were prepared using the PureYield Plasmid Midiprep System (Promega).

Cell Culture, Transfection, and Recording. HEK-293T cells (ATCC CRL-11268) were grown in Dulbecco's modified Eagle's medium supplemented with 10% fetal bovine serum (Thermo Fisher Scientific) and 1% penicillin/streptomycin (Thermo Fisher Scientific). Cells were maintained at 37 °C and supplemented with 5% CO_2. For transient transfections, Effectene (Qiagen) was used according to the manufacturer's protocol. To assess the activity of the Nav α-subunit alone, cells were transfected with the indicated Nav α-plasmid along with GFP vector as a cotransfection marker. Expression of the Nav α-subunit was validated by measuring a TTX-sensitive Na^+ current. Expression of cotransfected GFP- or DsRed-tagged β-subunits was validated by fluorescence microscopy prior to performing electrophysiological analysis. The current density before PR_{20} application was measured in each assay and used as the control for the current density after PR_{20} treatment.

Voltage clamping was performed using an EPC-10 amplifier (HEKA Instruments) at a sampling rate of 10 kHz filtered at 1 kHz. Data were acquired using an IBM-compatible computer running Patchmaster software (HEKA Instruments). The patch pipettes had a resistance of 2 to 3 MΩ when filled with the same pipette solution as in the I_{NaP} recording. The normal external solution (145 mM NaCl, 5 mM KCl, 10 mM Hepes, 1.25 mM NaH_2PO_4, 10 mM glucose, 1.2 mM $MgSO_4$, 1.8 mM $CaCl_2$, pH 7.3) was used for voltage-clamp recording. Current densities (pA/pF) were obtained after normalization to the cell surface area calculated by Patch master. Peak Na^+ channel currents were obtained by depolarizing pulses of 50 ms from −60 to +20 mV in 5-mV increments after a strong hyperpolarizing prepulse (−120 mV, 500 ms) for a full availability of Na^+ channels. Steady-state activation curves were obtained by transforming current data to conductance (G), which was calculated from the equation $G_{Na} = I/(V - E_{rev})$, where I is the peak Na^+ current density elicited by the depolarizing test potential, V is the test potential, and E_{rev} is the calculated Na^+ reversal potential. Steady-state activation data were fitted by Boltzmann function.

Purification of Recombinant Proteins. Recombinant protein of GFP:PR_{20} was purified as described previously (66). Briefly, bacterial expression plasmid for GFP:PR_{20} was transformed into *Escherichia coli* BL21 (DE3). The bacterial cells were grown in LB medium, and the expression of protein was induced by incubation with 0.5 mM Isopropyl β- d-1-thiogalactopyranoside (IPTG) at 16 °C overnight. For purification, cells were lysed in lysis buffer (50 mM tris(hydroxymethyl)aminomethane·hydrogen chloride (Tris·HCl), pH 7.5, 500 mM NaCl, 20 mM β-mercaptoethanol [BME], 1% Triton X-100, protease inhibitor mixture, 0.4 mg/mL lysozyme) by sonication at 60% power for 3 min. After centrifugation at 20,000 rpm for 90 min at 4 °C, the supernatants were mixed with nickel-nitrilotriacetic acid (Ni-NTA) resin (Qiagen) by gentle rocking at 4 °C for 30 min. The Ni-NTA resin was packed in a glass column (Bio-Rad) and then washed with 300 mL of wash buffer (20 mM Tris·HCl, pH 7.5, 500 mM NaCl, 20 mM imidazole, 20 mM BME, 0.1 mM Phenylmethylsulfonyl fluoride [PMSF]). The bound proteins were eluted from the resin using elution buffer (20 mM Tris·HCl, pH 7.5, 500 mM NaCl, 200 mM imidazole, 20 mM BME, 0.1 mM PMSF). Purified recombinant proteins were kept at −80 °C until use.

Immunoprecipitation and Western Blotting. For immunoprecipitation using brain slices, at first, V1 or M1 was incubated with 10 μM GFP:PR_{20} for 60 min. The samples were homogenized in 500 μL of IP buffer (50 mM Tris·HCl, pH 8.0, 150 mM NaCl, 1% Triton X-100, protease inhibitor mixture). After centrifugation at 4 °C for 20 min at maximum speed, the supernatants were collected and incubated with HA magnetic beads (Thermo Fisher Scientific) overnight at 4 °C. Upon three washes with ice-cold phosphate buffered saline (PBS), the immune complexes were eluted with 2× sodium dodecyl sulfate sample buffer and analyzed by western blotting. For western blotting, the eluted samples were separated using 4 to 12% NuPAGE Bis-Tris protein gels (Thermo Fisher Scientific), and the separated proteins were transferred onto nitrocellulose membrane and detected using indicated antibodies.

Immunohistochemistry. Brain slices were incubated with 100 nM GFP:PR_{20} in aCSF for 20 min at 32 °C and fixed with 4% paraformaldehyde in phosphate-buffered saline at room temperature overnight. After wash in PBS, the tissues were permeabilized using 0.5% Triton X-100 in PBS (PBS-T) for 30 min and incubated overnight at room temperature with anti-Nav1.2 (75-024; NeuroMab) or anti–Ankyrin G (sc-12719; Santa Cruz) antibodies. After a wash in 0.1% PBS-T, the tissues were incubated with Alexa Fluor 594–conjugated secondary antibody for 1 h and mounted with Vectashield Antifade Mounting Medium (Vector Labs).

Chemicals and Reagents. Reagents were obtained as follows: XE991, ZD7288, apamin, riluzole, D-AP5, SR-95531, CNQX, and TTX (Tocris); 4-AP (Sigma-Aldrich); and Effectene transfection reagent (Quiagen). Antibodies used and sources were as follows: anti-Nav1.2 antibody (ASC-002; Alomone); anti-Nav1.6 antibody (ASC-009; Alomone); anti-Nav β1-antibody (13950; Cell Signaling Technology); anti-Nav β2-antibody (ASC-007; Alomone); anti-Nav β4-antibody (Ab80539; Abcam); anti–β-Actin antibody (A5441; Sigma-Aldrich); anti–β-Tubulin antibody (2146; Cell Signaling Technology); HA (SC-7392; Santa Cruz); and HA magnetic beads (88837; Thermo Fisher). Anti-Nav1.2 antibodies specifically target short segments between domains I and II. Anti-Nav1.6 antibody specifically targets short segments between domains II and III. Anti-Nav

β1-antibody, anti-Nav β2-antibody, or anti-Nav β4-antibody specifically targets intracellular segments of each isoform.

Statistics. Data were analyzed with Igor Pro (Version 6.0; WaveMetrics) and Origin (Version 2020b; OriginLab). All results are presented as the mean ± SEM with the number of cells (*n*) used in each experiment. Statistical significance was evaluated using the Student's *t* test, and the level of significance was indicated by the number of marks. $P > 0.05$ was regarded as not significantly different. Comparisons between multifactorial statistical data were made using the two-way ANOVA. Normality was verified using the Shapiro–Wilk normality test and the Kolmogorov–Smirnov test.

Study Approval. Experimental procedures involving animals were approved by the Institutional Animal Care and Use Committee at Sungkyunkwan University School of Medicine (no. SKKUIACUC2020-08-42-1).

Data Availability. All study data are included in the article and/or *SI Appendix*.

ACKNOWLEDGMENTS. We thank Dr. Steven L. McKnight for valuable advice and critical comments on the composition of the manuscript and Dr. Gordon F. Tomaselli for providing the plasmids for human sodium channel subunits. This work was supported by National Research Foundation of Korea Grants NRF-2019R1A2C2003767 (to I.K.) and NRF-2020R1A2C2012846 (to H.C.).

1. M. DeJesus-Hernandez *et al.*, Expanded GGGGCC hexanucleotide repeat in noncoding region of C9ORF72 causes chromosome 9p-linked FTD and ALS. *Neuron* **72**, 245–256 (2011).
2. A. E. Renton *et al.*; ITALSGEN Consortium, A hexanucleotide repeat expansion in C9ORF72 is the cause of chromosome 9p21-linked ALS-FTD. *Neuron* **72**, 257–268 (2011).
3. G. Kim, O. Gautier, E. Tassoni-Tsuchida, X. R. Ma, A. D. Gitler, ALS genetics: Gains, losses, and implications for future therapies. *Neuron* **108**, 822–842 (2020).
4. T. F. Gendron, V. V. Belzil, Y. J. Zhang, L. Petrucelli, Mechanisms of toxicity in C9FTLD/ALS. *Acta Neuropathol.* **127**, 359–376 (2014).
5. I. Kwon *et al.*, Poly-dipeptides encoded by the C9orf72 repeats bind nucleoli, impede RNA biogenesis, and kill cells. *Science* **345**, 1139–1145 (2014).
6. S. Mizielinska *et al.*, C9orf72 repeat expansions cause neurodegeneration in Drosophila through arginine-rich proteins. *Science* **345**, 1192–1194 (2014).
7. R. Balendra, A. M. Isaacs, C9orf72-mediated ALS and FTD: Multiple pathways to disease. *Nat. Rev. Neurol.* **14**, 544–558 (2018).
8. C. Lagier-Tourenne *et al.*, Targeted degradation of sense and antisense C9orf72 RNA foci as therapy for ALS and frontotemporal degeneration. *Proc. Natl. Acad. Sci. U.S.A.* **110**, E4530–E4539 (2013).
9. K. Mori *et al.*, The C9orf72 GGGGCC repeat is translated into aggregating dipeptide-repeat proteins in FTLD/ALS. *Science* **339**, 1335–1338 (2013).
10. T. Zu *et al.*, RAN proteins and RNA foci from antisense transcripts in C9ORF72 ALS and frontotemporal dementia. *Proc. Natl. Acad. Sci. U.S.A.* **110**, E4968–E4977 (2013).
11. P. E. Ash *et al.*, Unconventional translation of C9ORF72 GGGGCC expansion generates insoluble polypeptides specific to c9FTD/ALS. *Neuron* **77**, 639–646 (2013).
12. C. J. Donnelly *et al.*, RNA toxicity from the ALS/FTD C9ORF72 expansion is mitigated by antisense intervention. *Neuron* **80**, 415–428 (2013).
13. S. Mizielinska *et al.*, C9orf72 frontotemporal lobar degeneration is characterised by frequent neuronal sense and antisense RNA foci. *Acta Neuropathol.* **126**, 845–857 (2013).
14. Y. Lin *et al.*, Toxic PR poly-dipeptides encoded by the C9orf72 repeat expansion target LC domain polymers. *Cell* **167**, 789–802.e12 (2016).
15. C. L. Lin *et al.*, Aberrant RNA processing in a neurodegenerative disease: The cause for absent EAAT2, a glutamate transporter, in amyotrophic lateral sclerosis. *Neuron* **20**, 589–602 (1998).
16. N. Geevasinga, P. Menon, P. H. Özdinler, M. C. Kiernan, S. Vucic, Pathophysiological and diagnostic implications of cortical dysfunction in ALS. *Nat. Rev. Neurol.* **12**, 651–661 (2016).
17. E. M. Perkins *et al.*, Altered network properties in C9ORF72 repeat expansion cortical neurons are due to synaptic dysfunction. *Mol. Neurodegener.* **16**, 13 (2021).
18. O. Schanz *et al.*, Cortical hyperexcitability in patients with C9ORF72 mutations: Relationship to phenotype. *Muscle Nerve* **54**, 264–269 (2016).
19. B. T. Selvaraj *et al.*, C9ORF72 repeat expansion causes vulnerability of motor neurons to Ca^{2+}-permeable AMPA receptor-mediated excitotoxicity. *Nat. Commun.* **9**, 347 (2018).
20. Z. I. Gunes, V. W. Y. Kan, X. Ye, S. Liebscher, Exciting complexity: The role of motor circuit elements in ALS pathophysiology. *Front. Neurosci.* **14**, 573 (2020).
21. A. C. Devlin *et al.*, Human iPSC-derived motoneurons harbouring TARDBP or C9ORF72 ALS mutations are dysfunctional despite maintaining viability. *Nat. Commun.* **6**, 5999 (2015).
22. B. P. Bean, The action potential in mammalian central neurons. *Nat. Rev. Neurosci.* **8**, 451–465 (2007).
23. K. Martinello, E. Giacalone, M. Migliore, D. A. Brown, M. M. Shah, The subthreshold-active K_V7 current regulates neurotransmission by limiting spike-induced Ca^{2+} influx in hippocampal mossy fiber synaptic terminals. *Commun. Biol.* **2**, 145 (2019).
24. M. C. Jiang, A. Adimula, D. Birch, C. J. Heckman, Hyperexcitability in synaptic and firing activities of spinal motoneurons in an adult mouse model of amyotrophic lateral sclerosis. *Neuroscience* **362**, 33–46 (2017).
25. W. Yu *et al.*, mGluR5-dependent modulation of dendritic excitability in CA1 pyramidal neurons mediated by enhancement of persistent Na^+ currents. *J. Physiol.* **596**, 4141–4156 (2018).
26. J. R. Paul *et al.*, Regulation of persistent sodium currents by glycogen synthase kinase 3 encodes daily rhythms of neuronal excitability. *Nat. Commun.* **7**, 13470 (2016).
27. W. Zhao *et al.*, Isoflurane modulates hippocampal cornu ammonis pyramidal neuron excitability by inhibition of both transient and persistent sodium currents in mice. *Anesthesiology* **131**, 94–104 (2019).
28. J. Lezmy *et al.*, M-current inhibition rapidly induces a unique CK2-dependent plasticity of the axon initial segment. *Proc. Natl. Acad. Sci. U.S.A.* **114**, E10234 (2017).
29. J. L. Pablo, G. S. Pitt, FGF14 is a regulator of KCNQ2/3 channels. *Proc. Natl. Acad. Sci. U.S.A.* **114**, 154–159 (2017).
30. J. Verneuil *et al.*, The M-current works in tandem with the persistent sodium current to set the speed of locomotion. *PLoS Biol.* **18**, e3000738 (2020).
31. J. Wang, S. W. Ou, Y. J. Wang, Distribution and function of voltage-gated sodium channels in the nervous system. *Channels (Austin)* **11**, 534–554 (2017).
32. J. M. Hull, L. L. Isom, Voltage-gated sodium channel β subunits: The power outside the pore in brain development and disease. *Neuropharmacology* **132**, 43–57 (2018).
33. W. Hu *et al.*, Distinct contributions of Na(v)1.6 and Na(v)1.2 in action potential initiation and backpropagation. *Nat. Neurosci.* **12**, 996–1002 (2009).
34. H. A. O'Malley, L. L. Isom, Sodium channel β subunits: Emerging targets in channelopathies. *Annu. Rev. Physiol.* **77**, 481–504 (2015).
35. A. Haustrate, A. Hantute-Ghesquier, N. Prevarskaya, V. Lehen'kyi, Monoclonal antibodies targeting ion channels and their therapeutic potential. *Front. Pharmacol.* **10**, 606 (2019).
36. H. Sun, M. Li, Antibody therapeutics targeting ion channels: Are we there yet? *Acta Pharmacol. Sin.* **34**, 199–204 (2013).
37. W. Zhao *et al.*, 1B50-1, a mAb raised against recurrent tumor cells, targets liver tumor-initiating cells by binding to the calcium channel α2δ1 subunit. *Cancer Cell* **23**, 541–556 (2013).
38. W. A. Catterall, Forty years of sodium channels: Structure, function, pharmacology, and epilepsy. *Neurochem. Res.* **42**, 2495–2504 (2017).
39. P. Vassilev, T. Scheuer, W. A. Catterall, Inhibition of inactivation of single sodium channels by a site-directed antibody. *Proc. Natl. Acad. Sci. U.S.A.* **86**, 8147–8151 (1989).
40. J. Gilchrist, S. Das, F. Van Petegem, F. Bosmans, Crystallographic insights into sodium-channel modulation by the β4 subunit. *Proc. Natl. Acad. Sci. U.S.A.* **110**, E5016–E5024 (2013).
41. W. Chen *et al.*, Neddylation stabilizes Nav1.1 to maintain interneuron excitability and prevent seizures in murine epilepsy models. *J. Clin. Invest.* **131**, e136956 (2021).
42. Y.-J. Zhang *et al.*, C9ORF72 poly(GA) aggregates sequester and impair HR23 and nucleocytoplasmic transport proteins. *Nat. Neurosci.* **19**, 668–677 (2016).
43. R. M. Clark, C. A. Blizzard, K. M. Young, A. E. King, T. C. Dickson, Calretinin and Neuropeptide Y interneurons are differentially altered in the motor cortex of the $SOD1^{G93A}$ mouse model of ALS. *Sci. Rep.* **7**, 44461 (2017).
44. C. S. Khademullah *et al.*, Cortical interneuron-mediated inhibition delays the onset of amyotrophic lateral sclerosis. *Brain* **143**, 800–810 (2020).
45. K. D. Thielsen *et al.*, The Wobbler mouse model of amyotrophic lateral sclerosis (ALS) displays hippocampal hyperexcitability, and reduced number of interneurons, but no presynaptic vesicle release impairments. *PLoS One* **8**, e82767 (2013).
46. H. Beck, Y. Yaari, Plasticity of intrinsic neuronal properties in CNS disorders. *Nat. Rev. Neurosci.* **9**, 357–369 (2008).
47. E. Jover, A. Massacrier, P. Cau, M. F. Martin, F. Couraud, The correlation between Na+ channel subunits and scorpion toxin-binding sites. A study in rat brain synaptosomes and in brain neurons developing in vitro. *J. Biol. Chem.* **263**, 1542–1548 (1988).
48. N. S. Gee *et al.*, The novel anticonvulsant drug, gabapentin (Neurontin), binds to the alpha2delta subunit of a calcium channel. *J. Biol. Chem.* **271**, 5768–5776 (1996).
49. S. Das, J. Gilchrist, F. Bosmans, F. Van Petegem, Binary architecture of the Nav1.2-β2 signaling complex. *eLife* **5**, e10960 (2016).
50. P. Delmas, D. A. Brown, Pathways modulating neural KCNQ/M (Kv7) potassium channels. *Nat. Rev. Neurosci.* **6**, 850–862 (2005).
51. T. J. Jentsch, Neuronal KCNQ potassium channels: Physiology and role in disease. *Nat. Rev. Neurosci.* **1**, 21–30 (2000).
52. D. A. Brown, G. M. Passmore, Neural KCNQ (Kv7) channels. *Br. J. Pharmacol.* **156**, 1185–1195 (2009).
53. B. C. Schroeder, C. Kubisch, V. Stein, T. J. Jentsch, Moderate loss of function of cyclic-AMP-modulated KCNQ2/KCNQ3 K+ channels causes epilepsy. *Nature* **396**, 687–690 (1998).
54. P. Li *et al.*, GABA-B controls persistent Na^+ current and coupled Na^+-activated K^+ current. *eNeuro* **4**, ENEURO.0114-17.2017 (2017).
55. M. C. Kiernan *et al.*, Amyotrophic lateral sclerosis. *Lancet* **377**, 942–955 (2011).
56. L. H. Goldstein, S. Abrahams, Changes in cognition and behaviour in amyotrophic lateral sclerosis: Nature of impairment and implications for assessment. *Lancet Neurol.* **12**, 368–380 (2013).
57. M. Ghasemi, R. H. Brown Jr., Genetics of amyotrophic lateral sclerosis. *Cold Spring Harb. Perspect. Med.* **8**, a024125 (2018).
58. H. Wood, A hexanucleotide repeat expansion in C9ORF72 links amyotrophic lateral sclerosis and frontotemporal dementia. *Nat. Rev. Neurol.* **7**, 595 (2011).
59. D. Radzicki, E. Liu, H. X. Deng, T. Siddique, M. Martina, Early impairment of synaptic and intrinsic excitability in mice expressing ALS/dementia-linked mutant UBQLN2. *Front. Cell. Neurosci.* **10**, 216 (2016).
60. J. F. Storm, Action potential repolarization and a fast after-hyperpolarization in rat hippocampal pyramidal cells. *J. Physiol.* **385**, 733–759 (1987).
61. M. R. White *et al.*, C9orf72 Poly(PR) dipeptide repeats disturb biomolecular phase separation and disrupt nucleolar function. *Mol. Cell* **74**, 713–728.e6 (2019).
62. P. McColgan, J. Joubert, S. J. Tabrizi, G. Rees, The human motor cortex microcircuit: Insights for neurodegenerative disease. *Nat. Rev. Neurosci.* **21**, 401–415 (2020).
63. H. L. Ball, P. Mascagni, Chemical synthesis and purification of proteins: A methodology. *Int. J. Pept. Protein Res.* **48**, 31–47 (1996).
64. J. Kim *et al.*, Changes in the excitability of neocortical neurons in a mouse model of amyotrophic lateral sclerosis are not specific to corticospinal neurons and are modulated by advancing disease. *J. Neurosci.* **37**, 9037–9053 (2017).
65. D. H. Feldman, C. Lossin, The Nav channel bench series: Plasmid preparation. *MethodsX* **1**, 6–11 (2014).
66. Y. Lin *et al.*, Toxic PR poly-dipeptides encoded by the C9orf72 repeat expansion target LC domain polymers. *Cell* **167**, 789–802.e712 (2016).